Spiral FFAG lattice design tools
Application to 6-D tracking

F. Méot [1] for the RACCAM Group

Abstract

Ray-tracing based methods for 3-D modeling of magnetic field and particle motion in spiral scaling FFAG accelerators have been developed. This allows efficient simulation of 6-D particle motion in presence of strong field non-linearities and possible field overlapping in configurations of neighboring magnets, thus yielding a performing tool for spiral FFAG lattice design and optimizations, and for 6-D tracking studies. It is applied for illustration to a principle design of, and simulation of an acceleration cycle in, a 200 MeV range (radiotherapy class) proton FFAG.

Key words: FFAG, spiral scaling FFAG, fixed field accelerator, 6-D tracking, fringe field, non-linear beam dynamics
PACS: 29.20.c, 29.27.a, 41.85.p

1 Introduction

Fixed field alternating gradient accelerators are nowadays subject to intense activities [1] in various domains as the acceleration of muons in the neutrino factory [2,3], hadrontherapy uses [4], high power beams [5], neutron production [6].

In the context of these collaborations, and in particular that of the RACCAM FFAG project[7], works have recently been undertaken concerning ray-tracing code developments regarding spiral FFAG lattice, in view of medical machine design in the short term, and possible application to muon rings for the scaling FFAG based neutrino factory [2] and other high-power beams, in the longer term.

A good knowledge of FFAG accelerator parameters can only be drawn from the single- or multi-turn stepwise ray-tracing. In particular this is the only method that allows computation of the dynamical acceptance of the ring. The developments presented here concern the implementation of such FFAG dedicated tools in the

[1] CEA DAPNIA & IN2P3 LPSC, F

1 June 2007

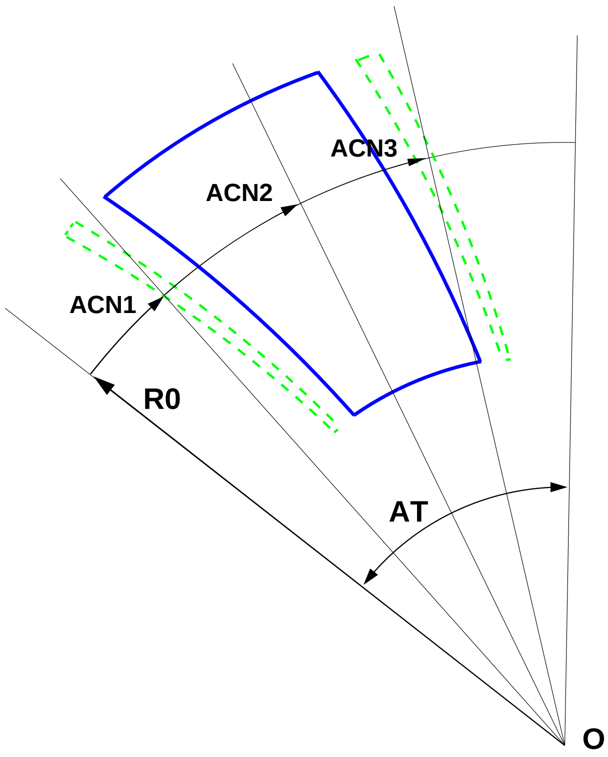

Fig. 1. Definition of a spiral FFAG magnet with clamps, using the "`FFAG-SPI`" procedure.

computer code Zgoubi [8]. This has various outcomes, as offering means for fast optimization of magnet geometry and fields as constrained by accelerator design parameters ; providing correct computation of periodic motion, tunes, amplitude and momentum detunings, time of flight, etc. ; yielding precision 6-D multiturn tracking and dynamic aperture tracking. In addition, preliminary adjustments of magnet/field parameters can be performed thanks to the built-in fitting procedure, whereas optimizations based on 3-D magnet code calculations have the inconvenience of being slow and lacking flexibility in that matter.

The paper is organized as follows. Section 2 describes the main ingredients and methods in the modeling of spiral FFAG magnets. Section 3 shows an application to design issues, from determination of first order parameters to full acceleration cycle, via dynamic aperture scan throughout the tune diagram.

2 A spiral magnet procedure

This Section describes the way the vertical field component $B_z(r, \theta)$ and derivatives at all position in the median plane of a magnet composed of N neighboring spiral field sectors (Fig. 1) with overlapping fields are calculated. The method is derived from an existing procedure regarding radial type FFAG magnets, presented in an earlier works [9], and yields a new routine, referred to as "`FFAG-SPI`" in the following.

The main ingredients are as follows. The magnetic field at (r, θ) in the median plane ($z = 0$) of a spiral sector is written

$$B_z(r, \theta) = B_{z0}\, \mathcal{F}(r, \theta)\, \mathcal{R}(r) \tag{1}$$

wherein B_{z0} is a reference field taken at a reference radius R_0 (Fig. 2). The factor $\mathcal{R}(r)$ models the r dependence of the field, and is written under the form

$$\mathcal{R}(r) = \left(\frac{r}{R_0}\right)^{k(r)} \quad \text{or} \quad \mathcal{R}(r) = b_0 + b_1 \frac{r - R_0}{R_0} + b_2 \left(\frac{r - R_0}{R_0}\right)^2 + ... \tag{2}$$

with $k(r)$ being the field index. Note that in the classical scaling FFAG optics k is in principle a constant, however it is allowed to be dependent of r in the present numerical approach : this permits designing possible compensation of the alteration of scaling properties under the effects of fringe field shape and extent, see below.

The magnet *EFBs* have a spiral geometry with equation $r = R_0 e^{b(r)\theta}$, with $b(r) = 1/\tan\xi(r)$ and $\xi(r)$ the spiral angle. In principle again, ξ is constant (logarithmic spiral), however we allow it to be dependent upon r, for the very reasons above of preserving scaling properties as linked to fringe field effects. The ensuing axial field form factor $\mathcal{F}(r, \theta)$ (often modelled by $\sin(N(\theta - \tan\xi \ln(r/r_0)))$, for a N-periodic ring, in analytical approaches [10]), gives the spiral azimuthal dependence of the field, and in the present ray-tracing tools is modelled in the way detailed below.

Field fall-offs The field fall-off (Fig. 3) at a particular effective field boundary (*EFB*) is written [11, p. 240]

$$\mathcal{F}_{EFB}(d) = \frac{1}{1 + \exp[p(d)])}\,, \quad p(d) = C_0 + C_1 d/g + \; ... \; + C_5 (d/g)^5 \tag{3}$$

wherein d is the distance to that *EFB* and depends on r and θ ($d_{En.}$ and $d_{Ex.}$ for respectively the entrance and exit *EFBs* in Fig. 2), and the normalizing coefficient g is normally homogeneous to the gap and can be a function of r, see below. The distance d is computed using a built-in numerical method that solves for θ the equation

$$\begin{aligned}(X_b - e^{b\theta} R_0 \cos(\omega + \theta))\,(b\, e^{b\theta} R_0 \cos(\omega + \theta) - e^{b\theta} R_0 \sin(\omega + \theta)) + \\ (Y_b - e^{b\theta} R_0 \sin(\omega + \theta))\,(e^{b\theta} R_0 \cos(\omega + \theta) + b\, e^{b\theta} R_0 \sin(\omega + \theta))\end{aligned} \tag{4}$$

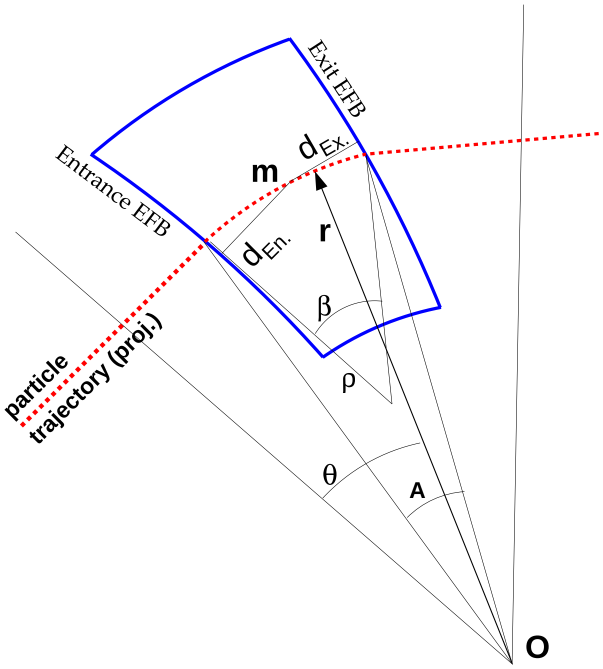

Fig. 2. Ingredients in computation of the axial field form factor.

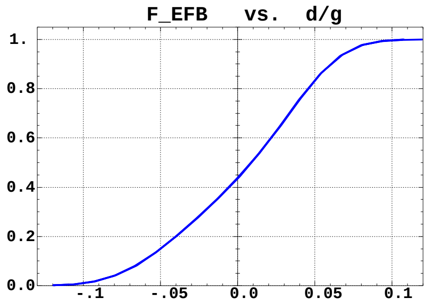

Fig. 3. Typical fringe field $\mathcal{F}_{EFB}(d/g)$ (Eq. 3).

which tells that the normal to the spiral EFB at location (x, y) on the spiral contains the observation (field) point (X_b, Y_b) (therein the angle ω is the EFB angular position in the reference frame). The numerical coefficients $C_0 - C_5$ are supposed to be known, for instance from prior matching with realistic fringe field data.

Noteworthy, an adequate positioning of the EFB makes possible to satisfy (referring to the frame as defined in Fig. 3)

$$\int_{d=-\infty}^{0} \mathcal{F}_{EFB}(u)\, du = \int_{d=0}^{\infty} (1 - \mathcal{F}_{EFB}(u))\, du$$

which entails that varying g (as ensuing from r dependence, for instance, Eq. 5) will not change the magnetic length, it will just change the fall-off steepness. This has the convenient consequence of allowing the simulation of various gap geometries as (see Section 3)

$$\begin{array}{llll} g(r) & = g_0(R_0/r)^\kappa, \quad \kappa \approx k & \text{gap shaping} & (5) \\ g(r) & = C^{st} \qquad (\kappa = 0) & \text{parallel gap} & \\ g(r) & = g_0\, r/R_0 \qquad (\kappa = -1) & \text{linear gap (constant vertical focusing)} & \end{array}$$

Both entrance and exit *EFBs* have their own fringe field factors, $\mathcal{F}_{\text{en.}}$, $\mathcal{F}_{\text{ex.}}$. The form factor at particle position (r, θ) is thus written

$$\mathcal{F}(r,\theta) = \mathcal{F}_{\text{en.}}(r,\theta) \times \mathcal{F}_{\text{ex.}}(r,\theta) \tag{6}$$

Full field at arbitrary position Now, accounting for N neighboring sectors (e.g., a central dipole and (possibly active) field clamps as in Fig. 2), the mid-plane field and field derivatives are computed by addition of the contributions of the $i = 1,\ N$ sectors taken separately, namely

$$B_z(r,\theta) = \sum_{i=1,N} B_{z0,i}\,\mathcal{F}_i(r,\theta)\,\mathcal{R}_i(r) \text{ and } \frac{\partial^{k+l}\vec{B}_z(r,\theta)}{\partial\theta^k\partial r^l} = \sum_{i=1,N} \frac{\partial^{k+l}\vec{B}_{zi}(r,\theta)}{\partial\theta^k\partial r^l} \tag{7}$$

Note that, in doing so it is not meant that field superposition does apply in reality, it is just meant to provide the possibility of obtaining a realistic field shape, that would for instance closely match (using adequate $C_0 - C_5$ sets of coefficients - Eq. 3) 3-D field distributions obtained from magnet codes or measurements. This procedure is illustrated in Fig. 4.

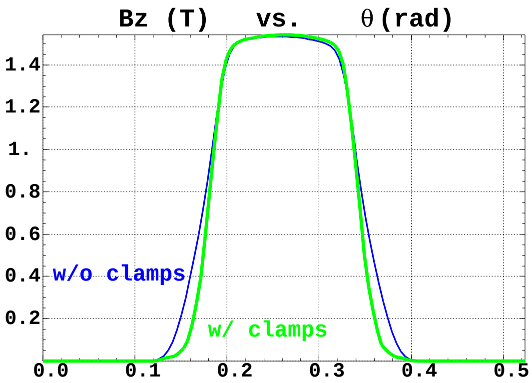

Fig. 4. Typical mid-plane field $B_z(r_0, \theta)$ (Eq. 7) as observed at traversal of a spiral sector equipped with two active magnetic shielding plates.

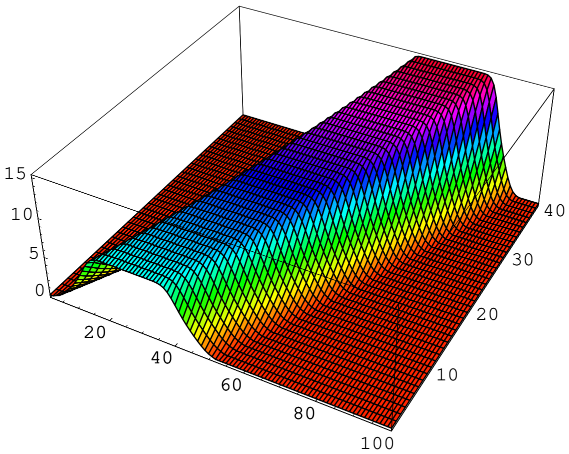

Fig. 5. Spiral magnet field map as obtained from Eqs. 1-7.

Eventually, the 6-D field model $\vec{B}(r, \theta, z)$ and derivatives $\partial^{k+l+m}\vec{B}/\partial r^k\partial\theta^l\partial z^m$ are deduced by z-extrapolation accounting for Maxwell equations [9,8].

Calculation of the mid-plane field derivatives (Eq. 7) can be done using two different methods, upon option, based respectively on
(i) numerical interpolation from a "flying mesh". In this case $B_z(r, \theta, Z = 0)$ is computed at the $n * n$ nodes ($n = 3$ or 5 in practice) of a "flying" interpolation mesh centered on the actual $(r, \theta, z = 0)$ particle position projection (m in Fig. 2).

(ii) use of a 2-D mid-plane magnetic field map, as shown in Fig. 5, that encompasses the all magnet, computed beforehand using the very procedure above.

In addition, a third method is under installation, fully based on analytical expressions of $B_z(r, \theta, Z)$ and derivatives $\partial^{i+j+k}/\partial r^i \partial\theta^j \partial z^k$.

The first method has the merit of allowing parameter optimization using the built-in "FIT" procedure. The second one has the merit of faster tracking. Both feature excellent symplecticity - dependent upon mesh size, integration step size. The third method has all the merits, speed, symplecticity, and it allows using "FIT".

3 Beam dynamics in a spiral ring

In this Section the code tools described above are tested, with the goal of showing that this spiral magnet modelling allied with stepwise ray-tracing method provides an efficient design tool. For that purpose a particular geometry, with given optical tuning, is submitted to various numerical experiments, as follows.

3.1 Introduction

The geometry and parameters of the lattice of concern are shown in Fig. 6. The magnets occupy a fraction ("packing factor") $pf = 0.4$ of the circumference, independent of radius, a scaling property. The extreme radii and rigidities satisfy, another scaling property, $B\rho_2 \ / \ B\rho_1 = (r_2/r_1)^{k+1}$. The dipole sector angle (18 deg.) and bend angle ($2\pi/8$, with 8 the number of cells) are in the ratio of pf.

Table 1
Parameters of the spiral ring.

number of cells	8	
field index k	3.50	
spiral angle ξ	50.0	(deg.)
packing factor pf	0.400	
min./max. radius $r_1 \ / \ r_2$	2.75 / 3.6	(m)
min./max. rigidity $B\rho_1 \ / \ B\rho_2$	0.6 / 2.	(T.m)
dipole sector angle	18.0	(deg.)
dipole bend angle	45.0	(deg.)

The smooth approximation of spiral scaling FFAG lattice allows deriving the optical functions with reasonable accuracy from matrix representation, with optical elements being the two side drifts, dipole ends wedge angles, and the dipole body (Fig. 7).

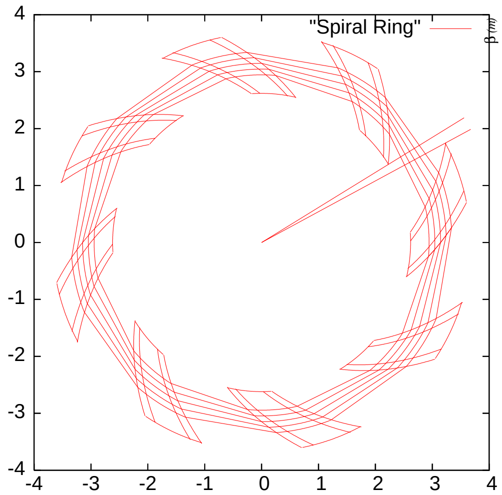

Fig. 6. Spiral ring and a set of closed orbits taken between 0.6 and 2 T.m.

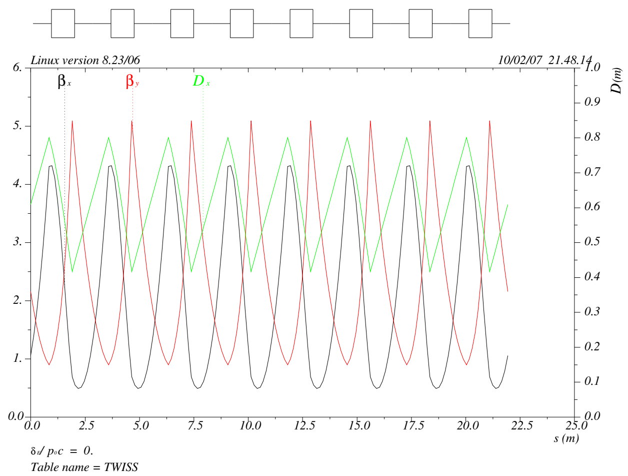

Fig. 7. Typical optical functions on closed orbits in the smooth approximation (at injection - they are similar with about 10% larger amplitude at extraction).

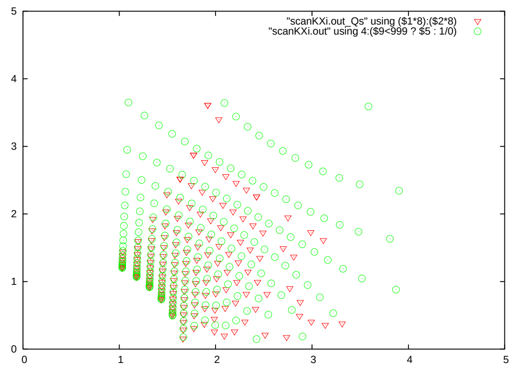

Fig. 8. Tune diagram showing the periodic stability region (circles : matrix transport, triangles : multiturn ray-tracing).

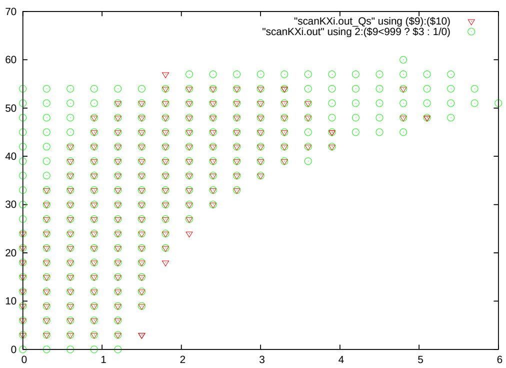

Fig. 9. k, ξ stability domain. Circles : matrix transport, triangles : multiturn ray-tracing.

This yields the periodic stability region shown in Fig. 8, and the corresponding (k, ξ) validity domain shown in Fig. 9.

Ray-tracing results over the region $\xi > 10$ deg. have been superimposed (crosses in Figs. 8, 9) - details on the method are given in App. 4. The agreement appears very good for lower k and ξ values and deteriorates with increasing k (this is attributed to the constant orbit radius approximation of the smooth approximation) and with increasing ξ (this is attributed to increasing perturbative effect of fringe fields). A large empty band around $Q_x = 2 + \frac{2}{3}$ can be observed in the ray-tracing case (Fig. 8), this corresponds to the systematic resonance line $3Q_x = 8$; in addition, the motion appears to be unstable at various (k, ξ) locations, detailed insight in phase-space motion generally shows coupling effects that entail large excursion and thus particle loss on walls.

It can be concluded at that stage that the consistency of the two types of results is good, whereas the precision of ray-tracing appears as expected necessary for further insight into the beam dynamics.

3.2 First order behavior

In the beam dynamics studies that follow we consider (arbitrarily) the particular optics $(k, \xi) = (3.5, 50\text{deg.})$ corresponding to tune values $(Q_x, Q_z) = (2.45, 1.78)$, with optical functions (on injection orbit) as shown in Fig. 7. The choice of this working point is arbitrary, it may appear too close to $2Q_x = 5$, however this is not a systematic resonance, so that it is not felt here.

This optics accounts for fringe field extent at magnet ends as represented in Fig. 3, with linear gap ($g_0 = 4$ cm, $R_0 = r_2 = 3.6$ m, $\kappa = k = 3.5$ in Eq. 5) thus yielding vertical tune $Q_z = 0.2218 \pm 10^{-4}$ independent of r, in addition to constant horizontal tune $Q_x = 0.3062 \pm 10^{-4}$ ensuing from scaling.

3.3 Large amplitude motion

This Section shows a series of simulations relevant to dynamic aperture tracking (Figs. 10, 11), amplitude detuning (Figs. 12-14) and to beam tune spread (Fig. 15).

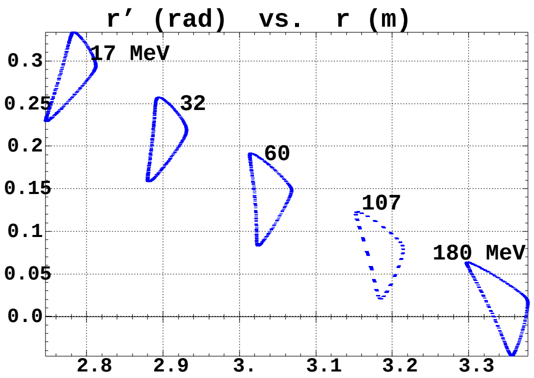

Fig. 10. Motion stability limits in horizontal phase-space, at 17, 80 and 180 MeV, either in the case of horizontal motion (the outer triangle) or in the presence of small vertical amplitude (inner triangle).

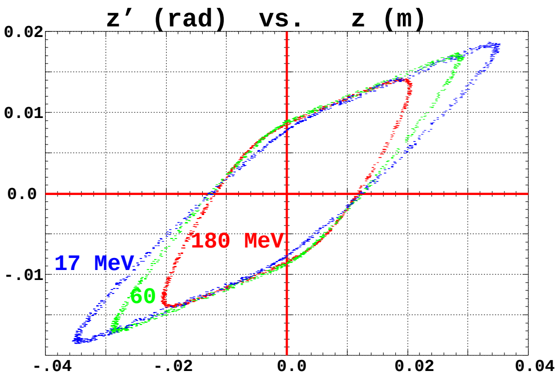

Fig. 11. Motion stability limits in vertical phase-space, at 17, 80 and 180 MeV, with horizontal motion in the neighboring of the closed orbit.

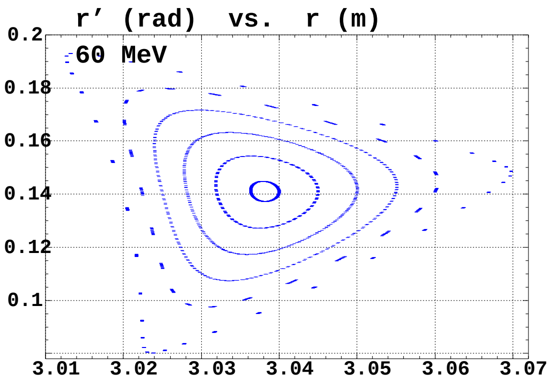

Fig. 12. Sample horizontal phase-space, from small amplitude to maximum stable amplitude, yielding tune versus amplitude dependence shown in Fig. 14.

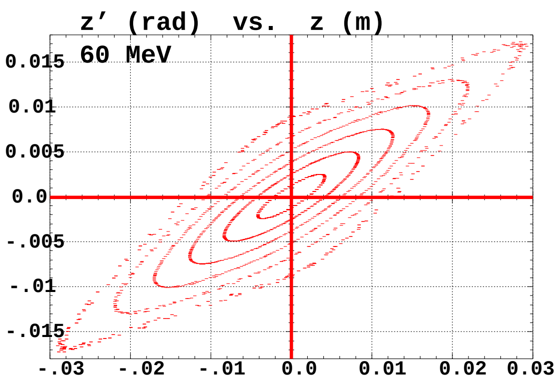

Fig. 13. Sample vertical phase-space, from small amplitude to maximum stable amplitude, yielding tune versus amplitude dependence shown in Fig. 14.

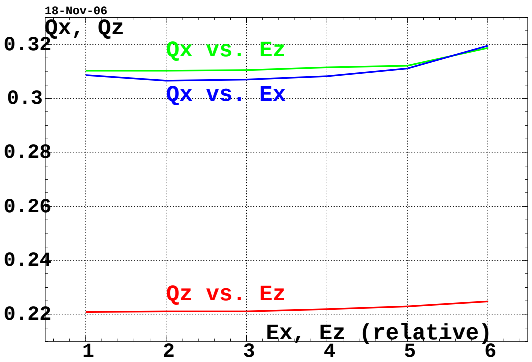

Fig. 14. Amplitude detuning, from paraxial motion up to maximum stable amplitude.

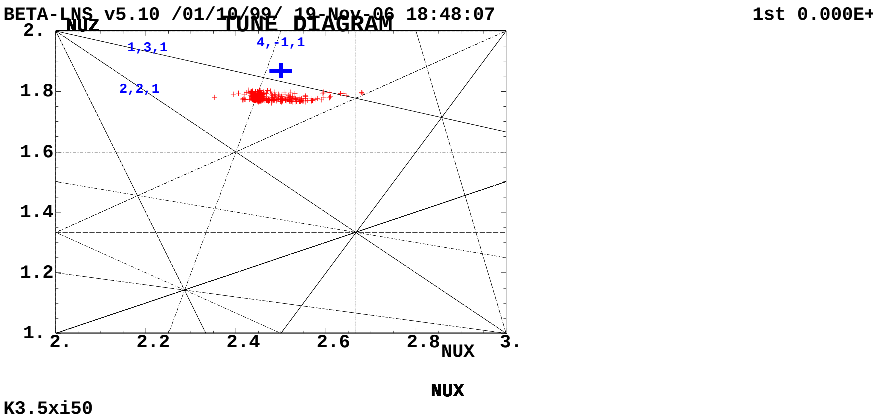

Fig. 15. Full beam occupation in tune diagram, due to sole amplitude detuning ($\delta p/p \equiv 0$). Right + skew lines, systematic, $m\nu_x + n\nu_z = 8p$, are shown.

4 Conclusion

Plans for future studies concern the acceleration and beam transmission.

On the other hand, the automatic procedure for finding the stability region (App. 4), that leads to Figs. 8, 9, will be extended to automatic search of dynamic aperture over the tune diagram. This will enable systematic analysis of DA in the working regions of interest, including in the effects of field and positioning errors.

Appendix - Motion stability region

An automatic procedure is used that loops on the parameters to be scanned, here k and ξ for getting the stable region in tune diagrams, and achieves the following, upon each loop :

(i) produce either a field map (as in Fig. 4) or the parameters for the `FFAG-SPI` procedure. This also produces the positioning of the magnet in absolute frame, and a set of approximate closed orbit coordinates, derived from the lattice cell geometry and corresponding to momenta taken between $B\rho_1 \times q/A$ and $B\rho_2 \times q/A$

(ii) find the exact closed orbits, starting from the approximate samples above, by multiturn ray-tracing : the closed orbit is at the center of the phase-space ellipse, for all momenta.

(iii) track paraxial radial and axial motions for this set of momenta, get the tunes by Fourier analysis. This last step provided the data as plotted in Figs. 8,9 in superimposition to the smooth approximation motion stability regions.

Note that, given the scaling optics, tunes are in principle independent of $B\rho$, hence should be the same over the all momentum sampling for a given pair (k, ξ). However sensible tune difference in the $B\rho_1 - B\rho_2$ range may appear under such effects as fringe fields for instance (e.g., for large spiral angles).

References

[1] The rebirth of the FFAG, M. Craddock, CERN Courrier 44-6 (2004) ; see also, Fixed field alternating gradient synchrotrons, F. Méot, Invited talk, ICFA-HB2004 Workshop, Bensheim, 18-22 Oct. 2004.

[2] A feasibility study of a neutrino factory in Japan, KEK report, Feb. 2001.

[3] USStudy2a

[4] Study of Compact Medical FFAG Accelerators, Toshiyuki Misu, FFAG04 workshop, KEK, Tsukuba, http://hadron.kek.jp/FFAG/FFAG04_HP/index.html.

[5] Accelerator Design and Construction for FFAG-KUCA ADSR, Yoshihiro Ishi, FFAG04 workshop, KEK, Tsukuba, http://hadron.kek.jp/FFAG/FFAG04_HP/index.html.

[6] ERIT, Y. Mori, NIM A (2006).

[7] The RACCAM Projetc, F. Méot et als., Proc. EPAC 2006 Conf.

[8] (a) The ray-tracing code Zgoubi, F. Méot, NIM A 427 (1999) 353-356, and also (b) Zgoubi users' guide, F. Méot and S. Valero, CEA DAPNIA SEA-97-13 and FERMILAB-TM-2010 (1997).

[9] F. Méot, F. Lemuet, Developments in the ray-tracing code Zgoubi for 6-D multiturn tracking in FFAG rings, NIM A 547 (2005) 638-651 ;
see also, Status of 6-D transmission simulations in FFAGs, F. Méot, FFAG05 Wrkshp, KURRI Institute, Kyoto, 5-9 Dec. 2005.

[10] FFAG Particle Accelerators, K. R. Symon et als., Phys. Rev. 103 (6), 1837 (1956).

[11] Deflecting magnets, H.A. Enge, in *Focusing of charged particles*, Vol. 2, A. Septier ed., Academic Press, New-York and London (1967).